The Nearby Type Ibn Supernova 2015G:
Signatures of Asymmetry and Progenitor Constraints

Isaac Shivvers,[1][*] WeiKang Zheng,[1] Schuyler D. Van Dyk,[2] Jon Mauerhan,[1]
Alexei V. Filippenko,[1] Nathan Smith,[3] Ryan J. Foley,[4] Paolo Mazzali,[5,6]
Atish Kamble,[7] Charles D. Kilpatrick,[4] Raffaella Margutti,[8] Heechan Yuk,[1,9]
Melissa L. Graham,[1,10] Patrick L. Kelly,[1] Jennifer Andrews,[3] Thomas Matheson,[11]
W. M. Wood-Vasey,[12] Kara A. Ponder,[12] Peter J. Brown,[13] Roger Chevalier,[14]
Dan Milisavljevic,[7] Maria Drout,[7,15] Jerod Parrent,[7] Alicia Soderberg,[7]
Chris Ashall,[6] Andrzej Piascik,[6] Simon Prentice[6]

[1]*Department of Astronomy, University of California, Berkeley, CA 94720-3411, USA*
[2]*IPAC, Caltech, Mail Code 100-22, Pasadena, CA 91125, USA*
[3]*Steward Observatory, University of Arizona, 933 N. Cherry Ave., Tucson, AZ 85721, USA*
[4]*Department of Astronomy and Astrophysics, University of California, Santa Cruz, CA 95064, USA*
[5]*Max-Planck-Institut für Astrophysik, Karl-Schwarzschild-Strasse 1, D-85748 Garching, Germany*
[6]*Astrophysics Research Institute, Liverpool John Moores University, Liverpool L3 5RF, UK*
[7]*Harvard-Smithsonian Center for Astrophysics, 60 Garden St., Cambridge, MA 02138, USA*
[8]*CIERA, Department of Physics and Astronomy, Northwestern University, Evanston, IL 60208, USA*
[9]*Department of Physics and Astronomy, San Francisco State University, San Francisco, CA 94132, USA*
[10]*Department of Astronomy, University of Washington, Box 351580, U.W., Seattle, WA 98195-1580, USA*
[11]*National Optical Astronomy Observatory, Tucson, AZ 85719, USA*
[12]*PACC, Physics and Astronomy Department, University of Pittsburgh, Pittsburgh, PA 15260, USA*
[13]*Department of Physics and Astronomy, Texas A&M University, 4242 TAMU, College Station, TX 77843, USA*
[14]*Department of Astronomy, University of Virginia, P.O. Box 400325, Charlottesville, VA 22904, USA*
[15]*Carnegie Observatories, 813 Santa Barbara Street, Pasadena, CA 91101, USA*

ABSTRACT

SN 2015G is the nearest known SN Ibn to date at $23.2\,\mathrm{Mpc}$ and it has proven itself a truly remarkable example of this rare subclass. We present the results of an extensive observational campaign including data from radio through ultraviolet wavelengths. SN 2015G was asymmetric, showing late-time nebular lines redshifted by $\sim 1000\,\mathrm{km\,s^{-1}}$. It shared many features with the prototypical SN Ibn 2006jc, including extremely strong He I emission lines and a late-time blue pseudocontinuum. The young SN 2015G showed narrow P-Cygni profiles of He I, but never in its evolution did it show any signature of hydrogen — arguing for a dense, ionized, and hydrogen-free circumstellar medium moving outward with a velocity of $\sim 1000\,\mathrm{km\,s^{-1}}$ and created by relatively recent mass loss from the progenitor star. Ultraviolet through infrared observations show that the fading SN 2015G (which was probably discovered some $20\,\mathrm{d}$ post-peak) had a spectral energy distribution that was well described by a simple, single-component blackbody. Archival *HST* images provide upper limits on the luminosity of SN 2015G's progenitor, while nondetections of any luminous radio afterglow and optical nondetections of outbursts over the past two decades provide constraints upon its mass-loss history.

Key words: supernovae: individual (SN 2015G) – stars: mass-loss

[*] E-mail: ishivvers@berkeley.edu

1   INTRODUCTION

A basic understanding of core-collapse supernovae (SNe) as luminous displays marking the collapse of a massive stellar core has been in place for at least half a century (e.g., Colgate & White 1966; Arnett 1971). Remarkably, new observations continue to find extreme examples of the process, some of which test the boundaries of our understanding.

For example, binarity within massive-star populations appears to produce complex and only partially understood diversity in supernova (SN) properties via pre-explosion mass exchange and mass loss, likely leading to the population of stripped-envelope SNe (Types IIb/Ib/Ic; e.g., Podsiadlowski et al. 1992; Smith et al. 2011; Sana et al. 2012; Shivvers et al. 2016a). Evidence is mounting from observations of interacting (Type IIn) SNe that their progenitors undergo extreme episodes of mass loss shortly before core collapse, creating dense circumstellar material (CSM; see review by Smith 2014), but exactly what mechanism is powering these death throes remains unclear. In some cases, enhanced (eruptive) mass loss occurs only a few years to decades before core collapse, which may point to instabilities in late nuclear burning phases triggering mass loss or binary interaction (e.g., Quataert & Shiode 2012; Mauerhan et al. 2013; Margutti et al. 2014; Smith & Arnett 2014).

Connecting the stripped-envelope and interacting SN populations are the rare Type Ibn SNe (e.g., Matheson et al. 2000; Foley et al. 2007; Pastorello et al. 2008a). These corecollapse SNe exhibit the narrow spectral emission lines characteristic of an ionized CSM and other key indications of dense CSM (e.g., Chugai 2009); however, spectra of SNe Ibn show little or no hydrogen emission and instead are dominated by strong helium emission lines (most notably He I $\lambda\lambda$5876, 6678, and 7065). Weak-hydrogen examples also exist as intermediate Type IIn/Ibn SNe (e.g., Pastorello et al. 2008b; Smith et al. 2012; Pastorello et al. 2015a), and there are a few known examples of hydrogen-weak explosions (Type Ib SNe) which then interacted with shells of hydrogen-rich material lost by the progenitor tens to thousands of years before core collapse (e.g., SNe 2001em and 2014C; Milisavljevic et al. 2015; Margutti et al. 2017).

Only about 20 SNe Ibn are known at this time, and the properties of this subclass are just beginning to be mapped out (e.g., Sanders et al. 2013; Pastorello et al. 2016; Shivvers et al. 2016b; Hosseinzadeh et al. 2017). SN 2015G, which exploded in the outskirts of NGC 6951[1] at a distance of 23.2 Mpc, is the nearest known SN Ibn to date; as such, it has allowed us the opportunity to study a member of this rare subclass in detail. In this paper we present the results of an extensive campaign from radio wavelengths to the ultraviolet (UV) and spanning nearly a year of follow-up observations. In §2 we present our observations, in §3 we put those data into context and calculate the implied physical properties of the system, and in §4 we summarise and conclude.

2   OBSERVATIONS

SN 2015G was discovered by Kunihiro Shima at 15.5 mag (unfiltered) on 2015-03-23.778 (we use UT dates and times throughout this article) and spectroscopically classified as a SN Ibn, similar to SN 2006jc, 3 s afterward (Yusa et al. 2015; Foley et al. 2015). We initiated a photometric and spectroscopic follow-up effort for SN 2015G as soon as its nature as a nearby example of the rare Type Ibn subclass was understood. From the ground, this campaign included a regular cadence of imaging through *BVRI* filters, a detailed spectroscopic follow-up campaign at both low and moderate resolution, two epochs of near-IR imaging (*J, H,* and *K$_s$* filters), and three epochs of radio-wavelength observations. We also obtained multiple epochs of space-based UV imaging with *Swift* and with the *Hubble Space Telescope (HST)*, three epochs of *HST* UV spectroscopy, and two epochs of *HST* optical imaging. Though some of these observations produced only nondetections, the combination of detections and upper limits forms an extensive dataset on SN 2015G.

Unfortunately, we did not catch SN 2015G before it reached peak brightness — comparisons between the early unfiltered amateur photometry and ours (beginning 4 d later) indicate that the SN was already on the decline at the time of discovery. Because the peak was unobserved, throughout this paper we refer to the time since the *discovery date* as the phase of SN 2015G.

2.1   Ultraviolet through Infrared Imaging

Filtered *BVRI* and unfiltered observations of SN 2015 were obtained with the 0.76 m Katzman Automatic Imaging Telescope (KAIT; Filippenko et al. 2001) at Lick Observatory nearly nightly from days 4 through 37. As the SN faded below KAIT's detection threshold, we began a campaign with the Direct Imaging Camera on the Lick 1 m Nickel telescope. We maintained a regular observing cadence until day 155, at which point SN 2015G faded below our Nickel detection threshold in both the *B* and *V* passbands.

Our images were reduced using a custom pipeline, as discussed by Ganeshalingam et al. (2010). Template subtractions were performed with additional images obtained on 12 July 2016 (day 477), after the SN had faded entirely. Point-spread-function (PSF) photometry was performed with the DAOPHOT package (Stetson 1987) in the IDL Astronomy User's Library.[2] Nearby reference stars in our images were calibrated to the APASS[3] catalog, which we transform to the Landolt system[4] and then to the KAIT4 natural systems using the colour terms and equations as calculated by Ganeshalingam et al. (2010, 2013). As the Nickel camera has aged, our best-fit colour terms for the above transformation have changed; we correct the data published here with updated Nickel colour terms recalculated in 2016 ($C_B = 0.041$, $C_V = 0.082$, $C_R = 0.092$, $C_I = -0.043$).

Table 1 presents our photometry of SN 2015G within the natural photometric systems of KAIT4/Nickel. Because

---

[1] NGC 6951 has also hosted two other SNe in the past few decades: SN IIn 1999el and SN Ia 2000E.

our observations show a significant gap in the bluer passbands, after the SN dropped below the sensitivity limits for KAIT in those passbands but before we began our campaign with the larger Nickel telescope, we do not convert these data into a standard photometric system. Ganeshalingam et al. (2010) and Ganeshalingam et al. (2013) provide the colour terms and equations required to perform this conversion, but doing so at all phases would require interpolating the evolution in the bluer passbands, so we provide only the natural photometry and leave any conversion (required for detailed comparisons with observations from other instruments) to future work.

Infrared (IR) imaging through the *J*, *H*, and *K$_s$* filters was obtained 18 s and 35 d after discovery with the Wisconsin-Indiana-Yale-NOAO (WIYN) 3.5 m telescope using the WIYN High-Resolution Infrared Camera (WHIRC; Meixner et al. 2008). SN 2015G was clearly detected in all three bands at both epochs. The raw images were processed using the methods described by Weyant et al. (2014) to construct the combined stacked images for each visit. We used Source Extractor to obtain aperture photometry, and we calculate photometric zeropoints for these data by crossmatching field stars with the Two Micron All Sky Survey catalog (2MASS; Skrutskie et al. 2006). We do not correct for any colour differences between the WIYN+WHIRC and 2MASS systems.

The Ultraviolet/Optical Telescope (UVOT; Roming et al. 2005) mounted on the *Swift* satellite (Gehrels et al. 2004) was used to observe the field of SN 2015G regularly from day 12 through day 30. Photometric reduction for these data was performed with the pipeline for the *Swift* Optical Ultraviolet Supernova Archive (SOUSA; Brown et al. 2014). For each of these images, a 5″ aperture is used to measure the counts for the coincidence loss correction, and a 3″ or 5″ source aperture (depending on the uncertainty from above) was used for the photometry after subtracting off the galaxy count rate in a template image. We apply aperture corrections (based on the average PSF in the *Swift* CALDB), zeropoint corrections, and time-dependent sensitivity loss corrections to place the magnitudes on the UVOT photometric system as described by Poole et al. (2008) and Breeveld et al. (2011). Most of these observations produced nondetections of SN 2015G, which prove useful in constraining the luminosity of SN 2015G at UV wavelengths.

The *HST* and its Wide Field Camera 3 (WFC3) was used to obtain optical images of SN 2015G through the *F555W* band on day 20 and the *F555W* and *F814W* bands on day 247, as part of programs GO-14149 (PI A. Filippenko) and GO-13683 (PI S. Van Dyk).[5] We also examine pre-explosion *HST* observations of the SN 2015G explosion site obtained in 2001 through the *F555W* and *F814W* filters with the Wide-Field Planetary Camera 2 (WFPC2) as part of the campaign to monitor SN 1999el (GO-8602 with PI A. Filippenko; see Li et al. 2002). All of these images were obtained from the *HST* Archive after standard pipeline pro-

[5] Another epoch of imaging was attempted on 15 October 2016 as part of GO-14668 (PI A. Filippenko), but unfortunately the observations were set up such that the pointing was toward the center of NGC 6951 and, owing to the orientation of the image array, the SN site itself was missed.

Table 1. Table of Photometric Observations

Date (UT)	Magnitude	Passband	Telescope
2015-03-27.51	17.07±0.07	B	KAIT
2015-03-27.51	16.61±0.04	V	KAIT
2015-03-27.51	16.20±0.03	R	KAIT
2015-03-27.51	15.81±0.04	I	KAIT
2015-03-28.53	17.17±0.08	B	KAIT
2015-03-28.53	16.71±0.04	V	KAIT
2015-03-28.53	16.30±0.03	R	KAIT
2015-03-28.53	15.86±0.04	I	KAIT
2015-03-29.54	17.25±0.15	B	KAIT
2015-03-29.54	16.77±0.08	V	KAIT
2015-03-29.54	16.40±0.05	R	KAIT
2015-03-29.54	15.94±0.08	I	KAIT
2015-03-30.52	17.63±0.02	B	Nickel
2015-03-30.52	16.94±0.01	V	Nickel
2015-03-30.53	16.44±0.01	R	Nickel
2015-03-30.53	15.99±0.01	I	Nickel
2015-03-31.53	17.63±0.21	B	KAIT
2015-03-31.54	17.10±0.07	V	KAIT
2015-03-31.54	16.61±0.05	R	KAIT
2015-03-31.54	16.09±0.06	I	KAIT

Truncated; full table available digitally.
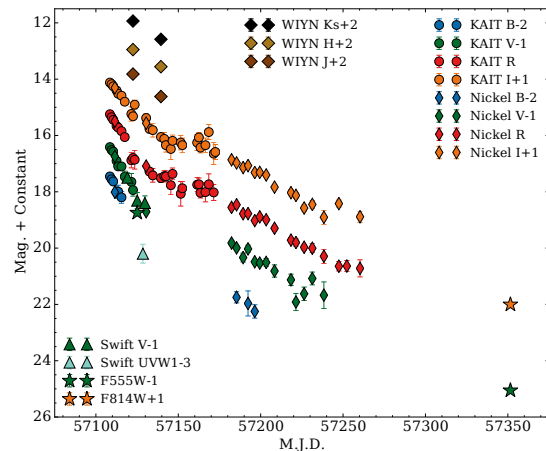
Figure 1. Our photometry of SN 2015G, from UV through IR wavelengths. All data are shown after correcting for extinction arising from dust within the Milky Way Galaxy and the SN host galaxy (see §2.4).

cessing. We performed photometry on these images using `DOLPHOT` (Dolphin 2000). The `DOLPHOT` parameters `FitSky` and `RAper` were set to 3 and 8 (respectively), appropriate for crowded galactic environments, and we set `InterpPS-Flib=1`, implemented with the TinyTim PSF library (Krist et al. 2011).

The above data are presented in Table 1 and shown in Figure 1. Values in the table are given as observed, without applying any dust reddening corrections. Additional UV-wavelength nondetections were obtained with *Swift*; we list only those relevant for this work.

Table 2. Table of Radio Observations

Date (UT)	Frequency (GHz)	3σ RMS (μJy)	VLA Configuration
2015-04-04.42	4.8	< 36.6	B
2015-04-04.42	7.1	< 34.8	B
2015-05-14.37	4.8	< 32.1	BnA
2015-05-14.37	7.1	< 37.8	BnA
2015-09-25.19	4.8	< 40.5	A
2015 Jul 25.19	7.1	< 29.8	A

2.2 Radio

We obtained three epochs of observations on SN 2015G using the Janksy Very Large Array (VLA), in April, May, and July 2015, all of which were nondetections producing upper limits on the radio flux from the SN.

All data were taken in the standard continuum-observing mode with a bandwidth of $16 \times 64 \times 2$ MHz. The VLA underwent a few configuration changes at various stages during these observations. During the data reductions, we split the data into two side bands of approximately 1 GHz each, centred on 4.8 and 7.1 GHz. We used the radio source 3C286 for flux calibration, and calibrator J2022+6136 for phase referencing. Data were reduced using standard packages within the Astronomical Image Processing System (AIPS). No radio emission was detected from SN 2015G in any of these observations, resulting in the deep flux limits summarised in Table 2.

2.3 Ultraviolet and Optical Spectra

Regular optical spectra of SN 2015G were obtained with the Kast Double Spectrograph mounted on the 3 m Shane telescope (Miller & Stone 1993) at Lick Observatory, starting day 3 (see Foley et al. 2015) and continuing until the SN was too faint for Kast. A single observation was taken with Kast in the spectropolarimetric mode, on day 4; the details of our spectropolarimetric observing techniques are described by Mauerhan et al. (2015) and Shivvers et al. (2016b). During the same time period we obtained additional spectra with the Boller & Chivens Spectrograph mounted on the 2.3 m Bok Telescope and the Spectrograph for the Rapid Acquisition of Transients (SPRAT; Piascik et al. 2014) mounted on the 2.0 m Liverpool Telescope. With these telescopes, we were able to maintain a cadence between observations of 1 week or less for the first 2 months of SN 2015G's evolution.

Several additional optical spectra were obtained after the SN had significantly faded using the DEep Imaging Multi-Object Spectrograph (DEIMOS; Faber et al. 2003) and the Low Resolution Imaging Spectrometer (LRIS; Oke et al. 1995; Rockosi et al. 2010) mounted on the Keck 10 m telescopes, the Multi-Object Double Spectrograph (MODS; Byard & O'Brien 2000) mounted on the 8.4 m Large Binocular Telescope (LBT), and the Bluechannel spectrograph on the 6.5 m Multiple Mirror Telescope (MMT), extending our spectroscopic sequence out until 16 September, some 6 months after SN 2015G was discovered.

All ground-based spectra were observed at the parallactic angle to minimise slit losses from atmospheric refrac-

tion (Filippenko 1982). We reduced and calibrated our Keck and Lick observations following the procedures detailed by Silverman et al. (2012), utilising IRAF[6] routines and custom Python and IDL codes.[7] For all Arizona facility telescopes (Bok, LBT, MMT), we performed standard reductions in IRAF. We use the standard reductions of SPRAT data as provided by the Liverpool automated pipeline. All data were flux calibrated via spectrophotometric standards observed through an airmass similar to that of SN 2015G, each night. We performed the spectropolarimetric reduction in the manner described by Mauerhan et al. (2015, and references therein), producing the reduced polarimetric parameters of q and u (Stokes parameters), P (debiased polarization), and θ (sky position angle).

As part of program GO-13797, we obtained three epochs of *HST*/Space Telescope Imaging Spectrograph (STIS) spectroscopy of SN 2015G (on 4, 11, and 20 April 2015) covering UV through near-IR wavelengths. We use the reduced spectra as provided by the Space Telescope Science Data Analysis System (STSDAS) pipeline.

Table 3 lists our spectra, and Figure 2 illustrates the spectral evolution of SN 2015G. All spectra will be made available for download through WISeREP[8], the Open Supernova Catalog[9] (Guillochon et al. 2016), and the UC Berkeley Supernova Database[10] (SNDB; Silverman et al. 2012).

2.4 Line-of-Sight Extinction

SN 2015G lies behind a moderate amount of dust extinction arising from the intestellar medium (ISM) within the Milky Way (MW): $E(B-V)_{MW} = 0.3189$ mag (Schlafly & Finkbeiner 2011). In our spectra that exhibit sufficient signal-to-noise ratio (SNR) and resolution, we observe an Na I D absorption doublet from gas within the MW, as well as Na I D from gas within the host galaxy NGC 6951 (see Figure 3).

We use these sodium doublets to estimate the extinction toward SN 2015G arising within the host galaxy. We measure the equivalent widths of the (separately resolved) D_1 and D_2 lines in both the MMT spectrum from 30 May and the Keck spectrum from 20 June, averaging multiple measurements from both spectra. We obtain 0.20 ± 0.06 and 0.37 ± 0.02 Å for D_1 and D_2, respectively. Assuming the dust and gas properties within NGC 6951 are well approximated by their properties within the MW ($R_V = 3.1$), we use the relations of Poznanski et al. (2012) to infer $E(B-V) = 0.053 \pm 0.028$ mag (using the D_1 line) and $E(B-V) = 0.076 \pm 0.028$ mag (using the D_2 line).

Given these measures, we estimate that NGC 6951 contributes $E(B-V) \approx 0.065$ mag, for a total line-of-sight dust reddening of $E(B-V) \approx 0.384$ mag. Our major results are not dependent upon the exact level of dust reddening, and we caution that our calculation of the internal host galaxy's reddening is only an estimate; the line-of-sight Na I D and dust

---

[6] IRAF is distributed by the National Optical Astronomy Observatory, which is operated by AURA, Inc., under a cooperative agreement with the NSF.
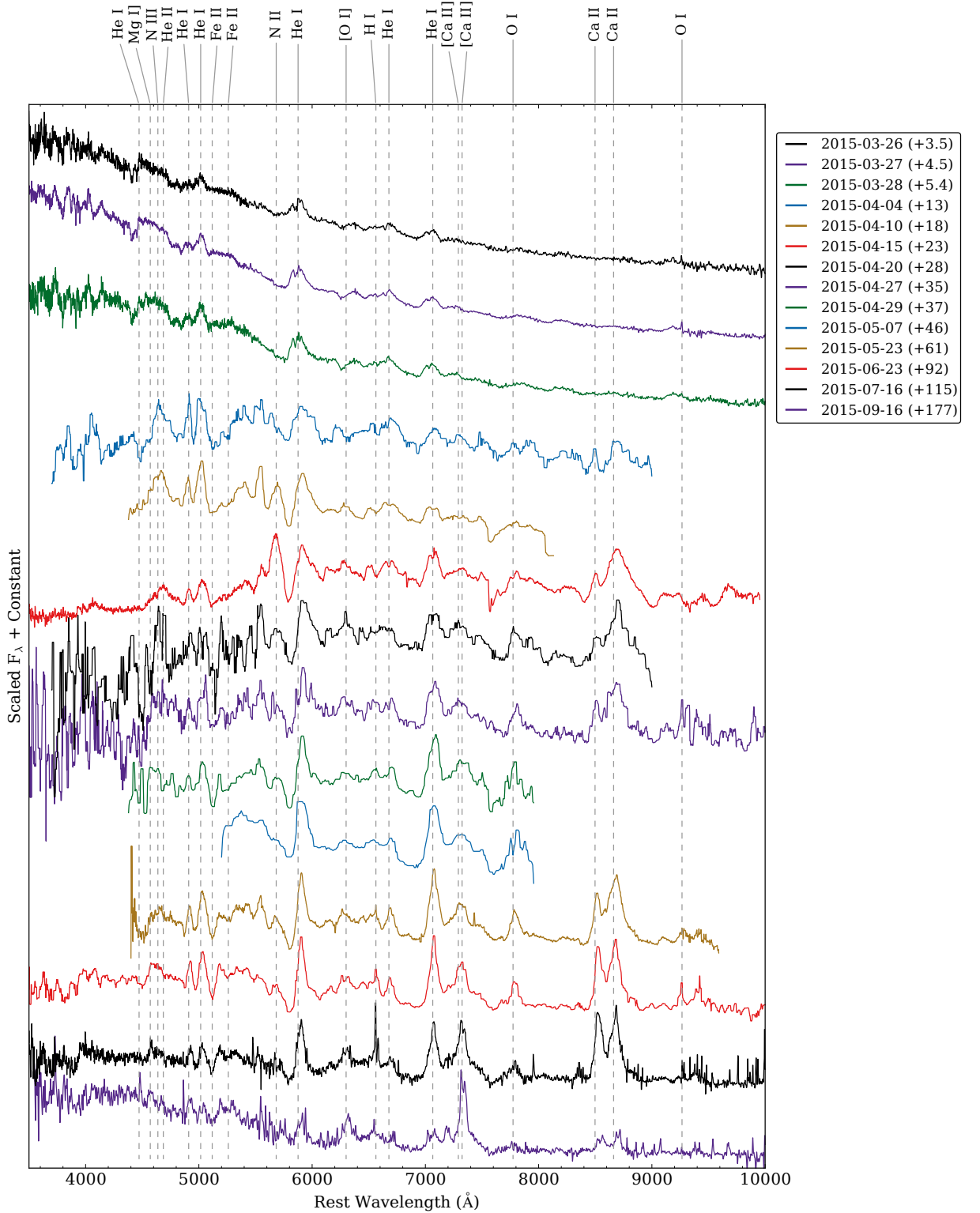[7] https://github.com/ishivvers/TheKastShiv
[8] wiserep.weizmann.ac.il
[9] sne.space
[10] heracles.astro.berkeley.edu/sndb

Figure 2. Subset of the observed spectral series, showing only the higher-SNR spectra for clarity. Our complete spectral dataset is listed in Table 3. Data have been corrected for dust absorption along the line of sight and are presented in the host galaxy's rest frame, and in the legend we state both the UT date of observation and the days since discovery. For some of the later epochs, we plot coadditions of multiple spectra to increase the SNR, and we label these coadditions with the mean date. Spectra at phases > 10 d have been smoothed via a moving window median or convolution with a Gaussian kernel. All line labels are plotted at the rest wavelenth of the line ($v = 0\,\mathrm{km\,s^{-1}}$).

Table 3. Journal of Spectroscopic Observations

Date (UT)	Tel./Inst.	Wavelength (Å)	Resolution (Å)
2015-03-26.51	Shane/Kast	3,450–10,860	10
2015-03-27.44	Bok/B&C	4,400–8,170	10
2015-03-27.50	Bok/B&C	6,190–7,350	2
2015-03-27.50	Shane/Kast	3,450–10,880	10
2015-03-28.46	Shane/Kast	3,460–10,850	10
2015-03-28.48	Shane/Kast	3,450–7,960	6
2015-03-28.50	Shane/Kast (SpecPol)	4,550–9,940	10
2015-04-04.64	HST/STIS/MAMA	1,570–10,230	10
2015-04-09	Liverpool/SPRAT	4,010–7,950	18
2015-04-10.49	Bok/B&C	5,700–6,870	2
2015-04-10.43	Bok/B&C	4,400–8,170	10
2015-04-11	Liverpool/SPRAT	4,010–7,950	18
2015-04-11.50	HST/STIS/MAMA	1,570–10,230	10
2015-04-15.44	LBT/MODS	3,500–10,000	7
2015-04-16.49	Shane/Kast	3,450–10,860	10
2015-04-17	Liverpool/SPRAT	4,010–7,950	18
2015-04-19.52	Shane/Kast	5,000–10,000	10
2015-04-20.31	HST/STIS/MAMA	1,570–10,230	10
2015-04-27	Liverpool/SPRAT	4,000–7,950	18
2015-04-27.43	Shane/Kast	3,500–10,500	10
2015-04-28.43	Bok/B&C	4,400–8,060	10
2015-04-29	Liverpool/SPRAT	4,020–7,990	18
2015-04-30.38	MMT/Blue Channel	5,710–7,000	2
2015-05-01	Liverpool/SPRAT	4,020–7,990	18
2015-05-05	Liverpool/SPRAT	4,020–7,990	18
2015-05-08	Liverpool/SPRAT	4,020–7,990	18
2015-05-10	Liverpool/SPRAT	4,020–7,990	18
2015-05-13	Liverpool/SPRAT	4,000–7,960	18
2015-05-20.56	Keck-2/DEIMOS	4,410–9,640	4
2015-05-26.48	Shane/Kast	3,460–10,880	10
2015-06-22.43	Shane/Kast	3,440–10,860	10
2015-06-23.47	Shane/Kast	3,450–10,850	10
2015-06-24.46	Shane/Kast	3,440–10,860	10
2015-07-16.53	Keck-1/LRIS	3,100–10,330	7
2015-07-20.37	Shane/Kast	3,430–10,820	10
2015-08-12.32	Shane/Kast	3,420–10,830	10
2015-09-16.38	Keck-1/LRIS	3,560–10,320	7

within the hosts of some previous SNe have been observed to be dissimilar from those of the MW (e.g., Phillips et al. 2013; Shivvers et al. 2016b).

3   ANALYSIS

We analyze all data in the rest frame of the host galaxy NGC 6951, adopting $z = 0.00475 \pm 0.000005$ (Haynes et al. 1998) and a distance of 23.2 Mpc ($\mu = 31.83$; median of 13 distances to NGC 6951 as reported on the Nasa Extragalactic Database[11]). Before our analysis we correct for absorption arising from dust both within our MW galaxy and within NGC 6951 (see §2.4).

3.1   SN 2015G's Spectral Evolution

Figure 2 illustrates the spectral evolution of SN 2015G. Hosseinzadeh et al. (2017) present four other spectra, providing additional coverage of the SN evolution between days

[11] `ned.ipac.caltech.edu/`

18 and 40. The early-time spectra of SN 2015G show the signatures observed in many young and intermediate-age SNe Ibn (e.g., Foley et al. 2007; Pastorello et al. 2008a; Hosseinzadeh et al. 2017). They have a strong continuum and relatively narrow P-Cygni helium lines (absorption minima blueshifted by $\sim 1000\,\mathrm{km\,s^{-1}}$) atop broader emission. By our third epoch of spectroscopy ($+5\,\mathrm{d}$), the broader emission lines formed a blueshifted absorption component, transforming into a P-Cygni line profile with absorption minima blueshifted by $\sim 8000\,\mathrm{km\,s^{-1}}$. These broader P-Cygni lines persisted throughout the photospheric phase and into the nebular phase, at which point the continuum had faded and the P-Cygni absorption components had disappeared, leaving behind the emission lines of helium and calcium which dominate our spectra out to the last observations.

SN 2015G's spectral features undergo a remarkable wavelength evolution over the course of our campaign, implying a similarly remarkable change in the velocity of the material contributing most to those features. Figure 4 shows this evolution for two HeI lines, for the forbidden doublet of [CaII] $\lambda\lambda 7291, 7324$ (which only becomes apparent start-
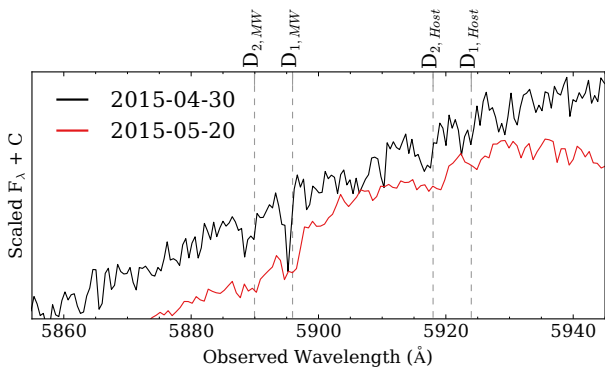
Figure 3. Na I D absorption lines observed in two of our higher-resolution spectra of SN 2015G, with the wavelengths of the doublet indicated in the Milky Way rest frame and in the rest frame of the host, NGC 6951.

ing ~ 100 d, but is prominent at late phases), and for the Ca II $\lambda\lambda$8498, 8542, 8662 near-IR triplet.

In the He I feature we see early P-Cygni absorption around $-1000 \, \mathrm{km \, s^{-1}}$ sitting atop broader emission lines with widths of $\sim 5000 \, \mathrm{km \, s^{-1}}$. Both the narrow and broad profiles at first show emission components centred near velocity $v = 0 \, \mathrm{km \, s^{-1}}$. By ~ 10 d, the major lines at wavelengths $\lambda \lesssim 6500$ Å (where the continuum is strongest) show broad, blueshifted P-Cygni absorption, as is normal in SN spectra. By ~ 20 d time the narrow P-Cygni features have faded from our spectra.

The SN then progresses toward the nebular phase and the continuum drops away below the emission lines. As it does so, the peaks of those emission lines clearly trend redward through our final observation. We model the near-IR calcium triplet in our last spectrum (+177 d) to measure its implied Doppler velocity. Our model consists of three Gaussian profiles separated by the triplet's intrinsic spacings and forced to have the same width, and we fit it to the data via Monte Carlo Markov Chain (MCMC) maximum-likelihood methods. Our best-fit profile is shown at the bottom right of Figure 4, and we find a velocity offset of $\sim 1000 \, \mathrm{km \, s^{-1}}$ receding (relative to the host-galaxy rest frame) and a full width at half-maximum intensity (FWHM) of $\sim 1400 \, \mathrm{km \, s^{-1}}$ (for each component line in the triplet). The forbidden calcium doublet can also be fit quite well by a doublet profile with an offset velocity forced to match that of the near-IR triplet, though we were required to allow the two components of the doublet to exhibit different FWHMs; perhaps the [O II] λ7320 blend is contributing some flux to the [Ca II] feature.

3.2 Comparisons with Other SNe

Figure 5 shows spectra of SN 2015G compared to those of other SNe Ibn and normal SNe Ib, with early-time spectra plotted on the left, late-time spectra on the right, and those taken at intermediate ages in the middle. We ran our +5 d spectrum of SN 2015G through the SuperNova Identification code (SNID; Blondin & Tonry 2007) with the updated template sets of Silverman et al. (2012) and Liu & Mod-

jaz (2014). Note that none of these template sets includes SN Ibn spectra, but SNID identified the +27 d SN Ib 2007C spectrum as a reasonable match. Broad features arising from many of the same ions are apparent in both SNe, though of course the SN 2007C spectrum (which is reasonably characteristic of normal SN Ib spectra at photospheric phases) does not exhibit the strong blue continuum and narrow emission features of SNe Ibn. The presence of a similar set of broad features between these two SNe suggests that SN 2015G could have been a relatively normal SN Ib if its dense CSM were not present.

The pre-maximum spectrum of SN 2015U showed emission lines of N II $\lambda\lambda$5680, 5686 and N III $\lambda\lambda$4634, 4642/C III λ4647 (Pastorello et al. 2015b; Shivvers et al. 2016b). Neither of these is apparent in our early spectra of SN 2015G. However, probable N II $\lambda\lambda$5680, 5686 and N III $\lambda\lambda$4634, 4642 emission features do become prominent by day 23 (see Figure 2).

During its transition from the photospheric phase to the nebular (see the middle panel of Figure 5), SN 2015G followed an evolution not so dissimilar from that of normal SNe Ib, as the previously dominant continuum faded away to leave only the nebular emission lines behind. However, the "broad" nebular features of SN 2015G are less broad than those shown by normal SNe Ib throughout, and the strong He I emission lines of SN 2015G do not appear in normal SN Ib spectra.

This strong He I emission is usually interpreted as a result of ongoing interaction between the outer layers of the ejecta and a helium-rich CSM (e.g., Matheson et al. 2000). Because the excitation energy of He I is so large, thermal excitation in the freely expanding and cooling SN ejecta cannot account for features like these. Instead, the ongoing shock between the ejecta and the helium-rich CSM is usually invoked to explain the strong helium lines in SNe Ibn. Normal SNe Ib, which show strong He I absorption lines at peak but no nebular He I emission lines, are often argued to arise via a different process: "mixed" SNe (e.g., Lucy 1991). In this scenario, radioactive nickel is mixed well out into the helium envelope and the γ rays from the decay process are therefore able to excite the helium nonthermally.

Hosseinzadeh et al. (2017) propose the existence of two spectroscopic subclasses of SNe Ibn: those that show narrow ($v \approx 1000 \, \mathrm{km \, s^{-1}}$) He I P-Cygni features within ~ 20 d of peak and those that do not. They group SN 2015U into the first class and they group both SNe 2006jc and 2015G into the second (SN 2014av, also shown in Figure 5, they label as intermediate between the classes). The spectra presented here show that the similarities between SNe 2015G and 2006jc are manifold and robust, but that SN 2015G actually did have narrow P-Cygni He I lines at early phases. SN 2015G therefore appears to span the differences between the two proposed subclasses (as SN 2014av does).

This adds evidence to the argument that either SNe Ibn exhibit a continuum of spectral properties between the two extremes exemplified by the Hosseinzadeh et al. (2017) subclasses, or that the issue of interest is not the presence or absence of narrow P-Cygni lines but instead their longevity or our viewing angle. Perhaps all SNe Ibn show these features but they quickly disappear from the spectra of SN 2006jc-like events, as those authors speculate, or perhaps SNe Ibn often exhibit strong asymmetries (in their CSM distribu-
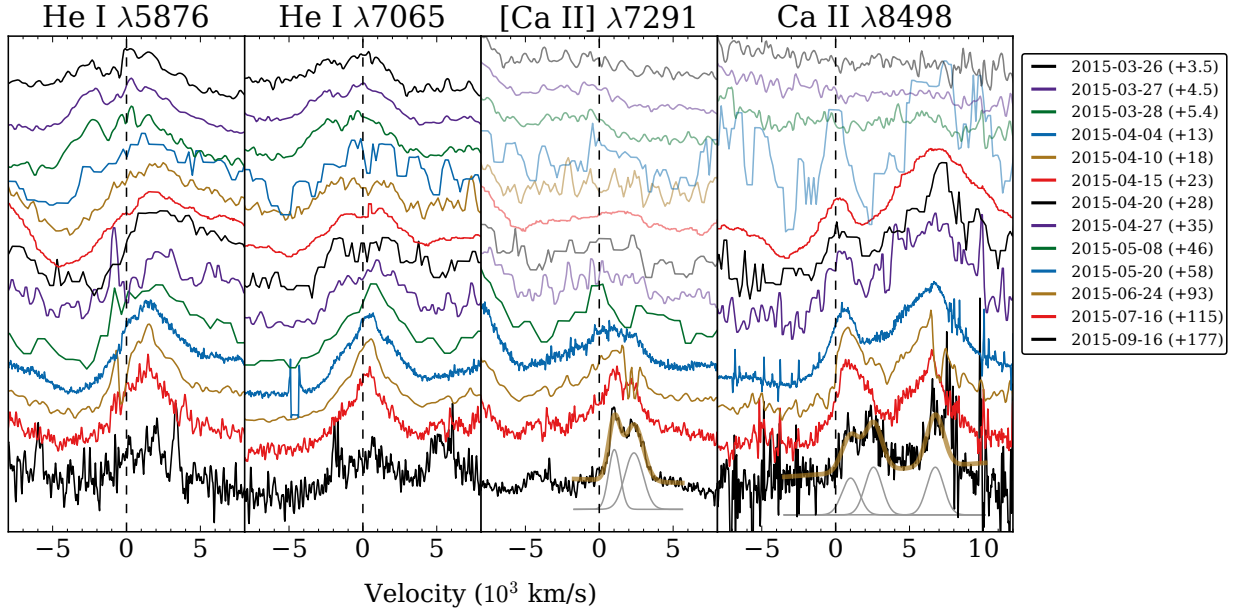
Figure 4. Evolution of He I, [Ca II], and Ca II lines in velocity space. All late-time lines are strongly offset redward from $0\,\mathrm{km\,s^{-1}}$, most clearly the Ca II. Note that we calculate velocities in both calcium panels relative to the blue-most line in each blend. Our best-fit line profiles of calcium features in the last spectrum are shown overlying that spectrum on the bottom, with the profile components shown below in grey.

tions or in their explosions) and the narrow lines are only apparent from certain perspectives.

SN 2015G exhibited much stronger calcium (both allowed and forbidden) than did SN 2014av, though comparisons to SN 2006jc indicate that the strength of these calcium features are quite variable among different objects. As the SNe Ibn shown in Figure 5 enter the nebular phase, their oxygen emission lines are weak compared to those of normal SNe Ib. The oxygen line strengths of SN 2015G are between those of the very oxygen-weak SN 2006jc and the oxygen-strong (normal) Type Ib SN 2004ao, at both mid-nebular and fully-nebular phases.

Note that the late-time spectra of SN 2015G show some similarities to those of the "calcium-rich" class of SNe Ib (see, e.g., Filippenko et al. 2003; Perets et al. 2010; Kasliwal et al. 2012; Foley 2015; Lunnan et al. 2017), with very strong calcium emission lines relative to those of oxygen. There are several important differences between SN 2015G and the calcium-rich SNe Ib, however, most notably the strong iron features (calcium-rich events show none in their spectra; Kasliwal et al. 2012).

As SN 2015G aged a blue continuum became apparent, similar to those observed in the Type Ibn SNe 1999cq and 2006jc (Matheson et al. 2000; Foley et al. 2007) and the transitional IIn/Ibn SN 2011hw (Smith et al. 2012), and visible in the right panel of Figure 5. The late-time blue continua of SNe 1999cq and 2006jc were attributed to a forest of blended Fe II lines; we believe the same process to be at work in the SN 2015G system. The density of features at these wavelengths makes individual lines difficult to isolate, but we identify clear Fe II features by comparing our 15 April spectrum to synthetic models calculated with

SYN++ (Fisher 2000; Thomas et al. 2011). We are unable to converge upon a SYN++ model that reproduces all of the major spectral features, most especially the strong He I emission, but our best-fit model does argue for significant near-UV line blanketing from iron as well as multiple overlapping absorption features in the blue, the two most obvious and isolated of which are indicated in Figure 2.

This blue pseudocontinuum arose later in SN 2015G's evolution than it did for SN 2006jc. Though the peak dates of both SNe passed by unobserved, the relative strengths of the Ca II and [Ca II] lines, as well as the O I and [O I] features, provide another indicator of the age. As the SN aged, forbidden emission lines became prominent while those lines arising from allowed transitions faded. The right-most panel of Figure 5 shows that the blue pseudocontinuum of SN 2006jc formed while the near-IR triplet of Ca II was strong, but the blue pseudocontinuum of SN 2015G did not become apparent until the near-IR triplet had faded and [Ca II] emission had become dominant (see also Figure 2). This enhanced blue continuum is generally understood to arise via non-thermal excitation of iron via an ongoing shock as ejecta collide with CSM (e.g., Foley et al. 2007), and normal SNe Ib do not show it.

SN 2006jc, at extremely late phases, developed a red/near-IR continuum as dust formed in the shocked shell of material created by the SN ejecta's collision with the CSM (Smith et al. 2008; Sakon et al. 2009). This red continuum is apparent in the +96 d spectrum of SN 2006jc; our spectra of SN 2015G show that no such late-time red continuum formed in SN 2015G during our 6 months of spectroscopic follow-up observations.

Interestingly, Smith et al. (2008) identified transient
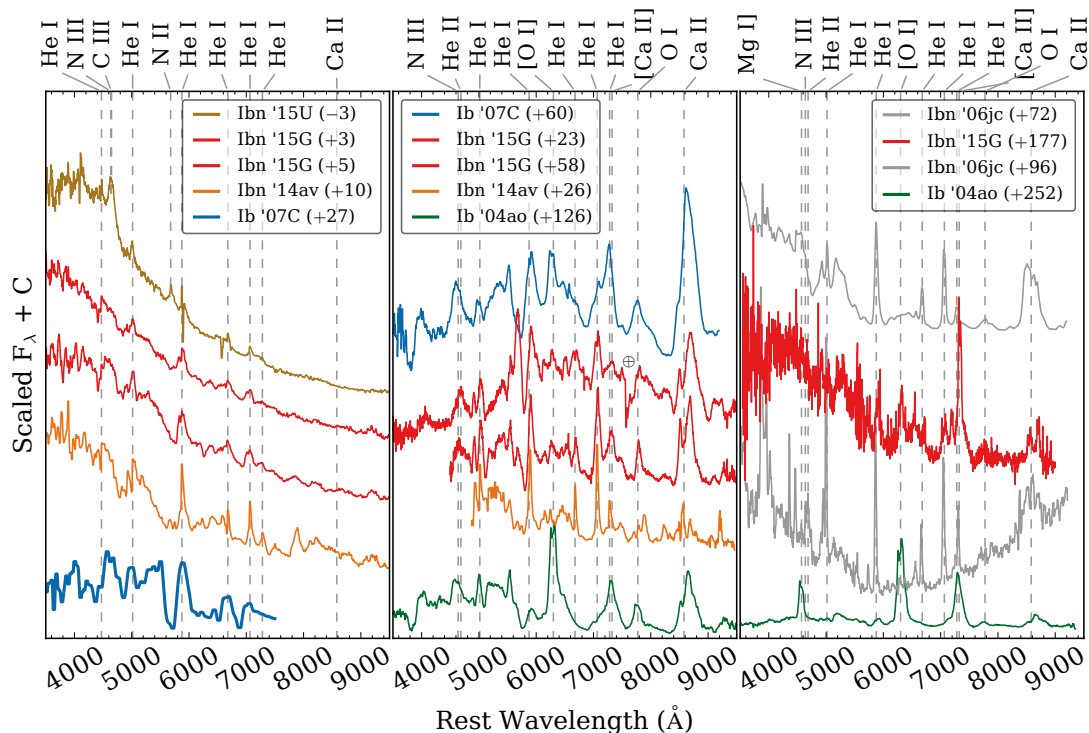
Figure 5. The spectra of SN 2015G at early, middling, and nebular phases (left, middle, and right panel, respectively). We compare to spectra of SNe Ibn 2006jc, 2014av, and 2015U (Foley et al. 2007; Smith et al. 2008; Pastorello et al. 2016; Shivvers et al. 2016b); to the SN Ib 2007C SNID template presented by Liu & Modjaz (2014) along with previously unpublished spectra of the event, and to previously unpublished spectra of SN Ib 2004ao. For each SN, spectra are presented in the SN rest frame and have been corrected for dust reddening along the line of sight. The phases of the spectra are given in days after discovery for SNe 2004ao, 2006jc, and 2015G, and days after optical peak for SNe 2007C, 2014av, and 2015U. All line labels are plotted at the rest wavelength of the line ($v = 0 \, \mathrm{km \, s^{-1}}$).

He II λ4686 and N III $\lambda\lambda$4634, 4642 emission with the rise of the red hot dust continuum of SN 2006jc, tying these phenomena to observations of the colliding winds in η Carinae (Smith 2010). The middle and right panels of Figure 5 show that the same transient emission feature of ionized helium and nitrogen was temporarily present in SN 2015G but at a much earlier phase, and it does not appear to be associated with the formation of dust in this event. Perhaps dust was able to form behind the shock in the SN 2006jc system, but not in SN 2015G, because the interaction occured in SN 2006jc only after the equilibrium temperature had dropped substantially. The spectra of SN 2015G showing He II and N III emission still exhibit a best-fit blackbody temperature of ~ 4000 K — likely too hot to allow any dust formation in the system at that phase.

Figure 6 shows the light curve of SN 2015G compared to template light curves for SNe Ib/c and Ibn (Li et al. 2011; Drout et al. 2011; Hosseinzadeh et al. 2017) and to the light curves of SNe Ibn 2006jc and 2015U (Foley et al. 2007; Shivvers et al. 2016b). The date of maximum brightness is unknown for both SNe 2006jc and 2015G; for this comparison we infer the dates of maximum for these two SNe by comparing their observed light curves to the template of Hosseinzadeh et al. (2017) while respecting the limits imposed by what constraints we have on their explosion dates. We

estimate that SN 2006jc was discovered some 6 d after peak and SN 2015G was discovered 20 d after peak.

The photometric evolution of SN 2015G is similar to that of other SNe Ibn (e.g., Pastorello et al. 2008a; Hosseinzadeh et al. 2017). Note, however, the steepening of SN 2006jc's R-band light curve around 75 d, likely caused by obscuration from a newly formed dust shell (Smith et al. 2008). In good agreement with our spectra, the light curve of SN 2015G shows no evidence for a forming dust shell at least out to ~ 8 months after discovery. Instead, the SN's optical light curve continues to decline approximately linearly and slightly more rapidly than the $^{56}\mathrm{Co} \rightarrow {}^{56}\mathrm{Fe}$ decline rate, as do those of normal SNe Ib.

Very few SNe Ibn have been monitored out to such late phases, so it is difficult to know how common the formation of a dust shell is among these events. However, enough have been observed to note that they show remarkable similarities in their post-peak light curves and, like SN 2015G, most SNe Ibn are subluminous at late phases compared to normal stripped-envelope SNe (Hosseinzadeh et al. 2017). If the luminosity of SNe Ibn on the post-peak decline is driven by radioactive decay, as is the case for normal stripped-envelope SNe, this implies that a significantly smaller amount of $^{56}\mathrm{Ni}$ is present in the ejecta of SNe Ibn than in those of normal SNe Ib/Ic.
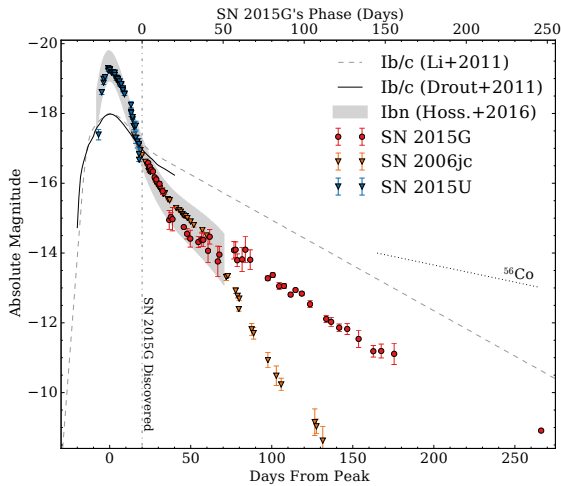
Figure 6. Absolute *R*-band light curve of SN 2015G, compared with absolute *R* light curves of SNe Ibn 2006jc (Foley et al. 2007; Maund et al. 2016) and 2015U (Shivvers et al. 2016b). We compare to the template light curves of Li et al. (2011, dashed line), Drout et al. (2011, solid line), and Hosseinzadeh et al. (2017, shaded region). We offset the SNe 2006jc and 2015G light curves so as to best match with the SN Ibn template, and we show the phase of SN 2015G relative to its discovery date on the top axis with the inferred phase relative to optical peak on the bottom axis. We also show the ^{56}Co $\rightarrow$ ^{56}Fe decline rate for comparison.

3.3 Spectropolarimetry

Our spectropolarimetric observation of the young SN 2015G is shown in Figure 7. SN 2015G shows strong continuum polarization ($P \approx 2.7\%$), with some small but apparently significant variations across the strong He I line features.

It is possible that the continuum polarization level is substantially affected or perhaps even dominated by interstellar polarization (ISP) along the line of sight. The host galaxy's contribution to interstellar dust absorption is relatively low and the SN appears to be in a rather remote environment, so we do not expect the host ISP to be dominant. Nonetheless, the maximum polarization from the host could be up to 0.6% (following Serkowski et al. 1975), with an entirely unknown position angle. The larger MW dust absorption toward SN 2015G indicates that our Galaxy's ISP contribution could be as high as 2.9% (Serkowski et al. 1975). Indeed, SN 2015G is at a low Galactic latitude of 14.8°, and substantial Galactic cirrus is present in this region of the sky.

The MW ISP can be estimated by measuring the polarization of stars that (1) are along the line of sight toward the SN (ideally within 1°); (2) are suspected to have negligible intrinsic polarization (ideally spectral types A5 through F5; Leonard et al. 2002); and (3) lie at sufficient distances such that all ISM along the line of sight and within a scale height of 150 pc above the Galactic disk is sampled. For the line of sight near SN 2015G this minimum required probe distance is 675 pc. Unfortunately, there are no stars in the literature of known spectral type with polarization measurements satisfying all of these criteria. Loosening these constraints to allow stars of any spectral types within 5°, we identify two stars
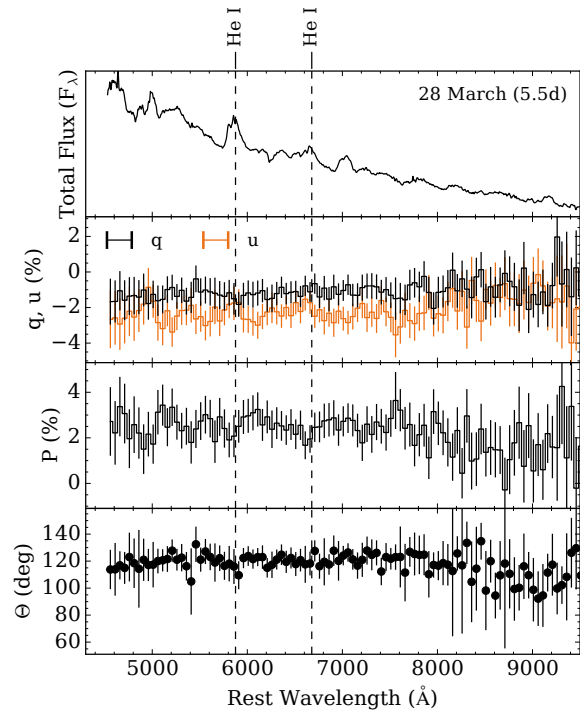
Figure 7. A single epoch of spectropolarimetry obtained 5.5 d after the discovery of SN 2015G. The top panel illustrates the total-flux spectrum smoothed with a 50 Å Gaussian kernel, while the middle panels show the Stokes parameters (q,u) and total polarization (P) binned to 50 Å, and the bottom panel gives the measured position angle, also binned to 50 Å.

in the catalog of Heiles (2000) — HD 197911 (B5 V; 1043 pc) and HD 198781 (B0.5 V; 712 pc) — which exhibit an average (1σ) polarization and position angle of 1.36% (0.03%) and 150° (16°). This position angle value is consistent with that measured for SN 2015G, while the level of polarization is about half that of the SN. However, we are reluctant to trust these values as accurate measures of the ISP because at least one of those stars (HD 197911) has been associated with a dusty interstellar bow shock that is likely to scatter the star's light and exhibit its own polarization (Peri et al. 2015). The existence of a star at that distance (well beyond the 675 pc limit we imposed above) with shocked ISM in its vicinity suggests that the scattering and polarizing effect of the ISM could extend to distances larger than expected in this region of the sky, and may be highly spatially variable.

To improve our census of the ISP, we obtained new Lick/Kast observations (on 2017 March 3) of two additional probe stars of known spectral types that have smaller angular separations, $< 2°$: BD 661309 (A5 V) exhibits $P_V = 0.22(0.01)\%$ and $\theta_V = 54.7°(1.0°)$, and HD 197344 (B8 V) exhibits $P_V = 0.22(0.01)\%$ and $\theta_V = 64.6°(1.2°)$. These stars have spectroscopic parallaxes that indicate distances of 525 and 575 pc, respectively — close to, but slightly below, the minimum suggested distance to effectively probe the bulk of intervening ISM. Nonetheless, the measured values are very low, which indicates that either the ISP is small near the SN's line of sight or that there is substantial ISP originating from greater distances than we are currently able to probe.

In conclusion, the complexity of the ISM in this region of the sky and the lack of excellent probe stars has proven problematic for our efforts to obtain a reliable estimate of the ISP toward SN 2015G. However, we note that none of the ISP estimates we have considered come close in strength to the very strong ~ 2.7% measured for the SN. It appears that, if the SN is not intrinsically polarized, then the ISP vector components of the MW and the host must be constructively interfering (i.e., have similar position angles, or at least be in similar quadrant of the $q-u$ plane) to give us such a strong polarization measure. For this reason, it seems plausible that the intrinsic polarization of the SN is significant and, therefore, that the electron-scattering photosphere of the explosion is substantially aspherical, consistent with the other proxies for explosion asymmetry we consider in this paper. Without better constraints on the ISP, however, it is difficult to quantify the degree of asphericity.

3.4 The Ultraviolet Spectra

Figure 8 shows the full STIS UV+optical spectrum from day 13, rebinned and median-averaged in wavelength bins ~ 50 Å wide to increase the SNR and reduce the effects of cosmic rays. Continuum emission is detected from ~ 2300 Å out to ~ 1 μm, overlain by the broad and narrow P-Cygni features described above. We find one emission line in the near-UV, labeled Mg II λλ2796, 2803 in Figure 8. This feature is also observed in our spectrum from 11 April, but not in the spectrum from 20 April (at which point the continuum has faded below detectability at these wavelengths as well). Between the first two spectra it evolves from a wavelength of 2764 ± 2 Å to 2784 ± 6 Å (uncertainty estimated via MCMC fits of two Gaussian profiles separated by the spacing of this doublet, 7.16 Å). Assuming our line identification is correct, and that both lines of the doublet contribute equally to the line flux, this implies velocity blueshifts for this feature of about $3800 \, \mathrm{km \, s^{-1}}$ and $1600 \, \mathrm{km \, s^{-1}}$ on 4 and 11 April (respectively), so the slowdown is $\sim 300 \, \mathrm{km \, s^{-1} \, d^{-1}}$. No other narrow emission lines in our dataset on SN 2015G show this sort of behaviour and we note that it is peculiar. However, the SNR is low in our UV spectra and, though inspection of the raw two-dimensional frames shows them to be clean with no obvious artifacts, we are hesitant to infer too much from this putative Mg II line.

3.5 The Spectral Energy Distribution

Our observations of SN 2015G cover radio through UV wavelengths, and we are able to reconstruct a broad-wavelength spectral energy distribution (SED) at several phases. Figure 9 shows the UV through IR SED of SN 2015G as observed at 5 epochs between 12 d and 35 d after discovery. For the two phases at which we have IR photometry, we interpolate the optical light curves to the time of the IR observations using a Gaussian process regression. At the earlier epoch, the *Swift* satellite observed the location of SN 2015G nearly concurrently (within a few hours), and we plot the 3σ upper limits from the resulting UV nondetections. For the later epoch we plot the last UV nondetection from *Swift*, which was observed 5 d before the listed phase (when the optical+IR images were taken).

Our *HST* spectra strongly constrain the wavelength of peak flux, and we show a best-fit model blackbody spectrum in Figure 9, for comparison. Fitting a redshifted and dust-reddened blackbody (assuming the dust properties presented in §2.4) to the first *HST* spectrum, we find that the SED of SN 2015G is approximated quite well by a single-component blackbody with a temperature of $T_{\mathrm{BB}} \approx 5470 \pm 250$ K. Our uncertainties about the dust reddening arising within the host galaxy likely dominate our temperature errors, so we estimate the above error bars on T_{BB} by ranging $E(B-V)_{\mathrm{host}}$ from 0.0 mag to twice our best-guess value of 0.065 mag and refitting. For Figure 9 we have converted our photometric observations into flux units using PySynphot and the published filter curves for each instrument, assuming a 5470 K blackbody spectrum.

Between 12 d and 35 d after discovery, the SED qualitatively behaves like a cooling blackbody, fading in both temperature and luminosity. Our IR photometry argues for a steeper Rayleigh-Jeans tail than do our fits to the UV/optical peak, but (given our uncertainties about the degree and wavelength dependence of the dust obscuration toward SN 2015G) we are hesitant to assign much significance to that discrepancy. We estimate the bolometric energy output of SN 2015G and the implied blackbody radius at 11.9 d after discovery, based upon our blackbody fit to the *HST* spectrum: $L \approx 10^{42} \, \mathrm{erg \, s^{-1}}$ and $R \approx 10^{15}$ cm.

3.6 Limits on Radio Luminosity

Radio emission from SNe predominantly arises via the synchrotron mechanism as the forward shock ploughs through the CSM. The narrow emission features in our early-time optical spectra provide clear evidence for a dense CSM near the progenitor at the time of core collapse. However, the density profile of the CSM at larger radii is quite uncertain, so the radio flux expected from the SN at intermediate and late phases is similarly uncertain. Though our attempts to observe radio emission SN 2015G yielded only upper limits, they do provide some interesting constraints on the extended CSM surrounding the SN.

We argue elsewhere in this paper that the dense CSM that made SN 2015G a SN Ibn was likely not created by wind-like mass loss from the progenitor, but rather was built up through one or more extreme mass-loss events $\lesssim 1$ yr before core collapse. However, we find it plausible (in the absence of evidence to the contrary) to assume a history of more stable wind-like mass loss from the progenitor at earlier times before core collapse, as is normal for the progenitors of stripped-envelope SNe (e.g., Chevalier 1998; Kamble et al. 2014, 2016).

Our mid-phase spectra show broad lines with absorption edges falling at blueshifts of $\sim 8000 \, \mathrm{km \, s^{-1}}$ (see Figure 4), placing a lower limit on the velocity of the forward shock ($v_{\mathrm{shock}} \gtrsim 8000 \, \mathrm{km \, s^{-1}}$), while the narrow P-Cygni features in our early-time spectra have characteristic velocities of $1000 \, \mathrm{km \, s^{-1}}$. We construct a simple model of the SN 2015G system by assuming a history of mass loss with $v_{wind} \approx 1000 \, \mathrm{km \, s^{-1}}$ and adopting $v_{\mathrm{shock}} = 10,000 \, \mathrm{km \, s^{-1}}$. We further estimate that the SN took ~ 5 d to rise to maximum (SN 2015G's rise time is effectively unconstrained, but other SNe Ibn for which the rise has been observed exhibit values of ~ 5 d; Hosseinzadeh et al. 2017), giving a best-guess date
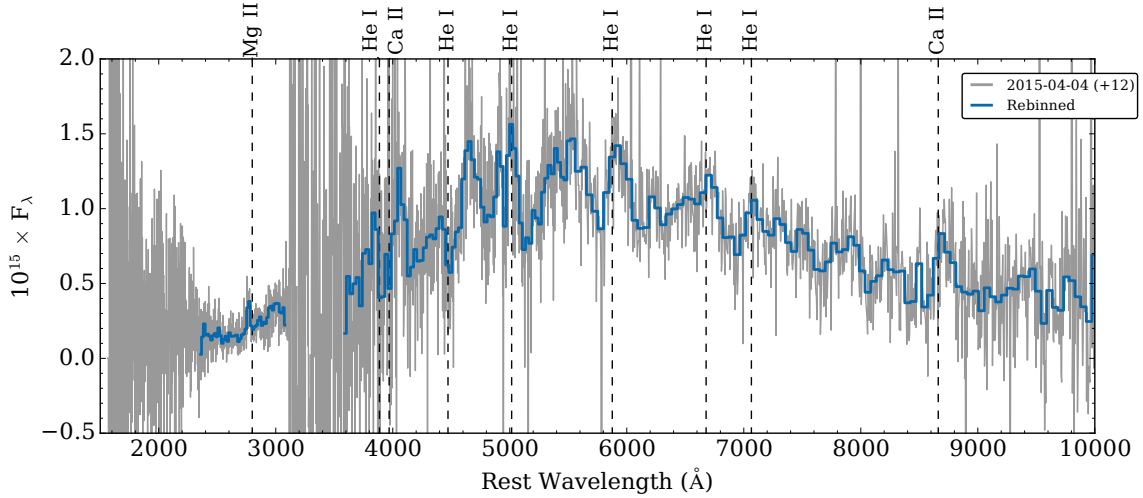
Figure 8. The UV through near-IR spectrum of SN 2015G, as observed by *HST*. Data have been corrected for dust absorption along the line of sight and are presented in the host galaxy's rest frame. The full spectrum is shown in grey and a rebinned spectrum with bins ~ 50 Å wide is shown in blue.
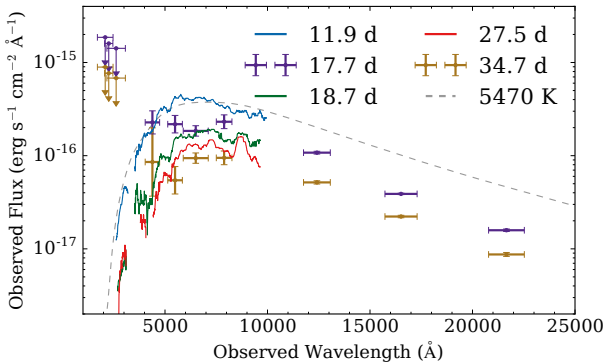
Figure 9. UV through IR observations of SN 2015G, including three UV-optical spectra observed by *HST*, which have been trimmed and smoothed with a wide (~ 500 Å) median box filter to illustrate the overall SED, alongside two epochs of UV–IR photometry. All data are shown in the observer frame, with no corrections for extinction applied. For comparison, a blackbody at 5470 K is shown in dashed grey, redshifted into the observer's frame and obscured by the dust populations described in §2.4. Phase (days) or T_{BB} (K) are given in the legend.

of explosion of 2015-02-27. Our naive blackbody model from §3.5 showed that our data are described rather well by a cooling blackbody of $R \approx 10^{15}$ cm. If we take this value to be the outer extent of the low-radii dense CSM, the forward shock would have taken ~ 10 d to traverse this inner CSM and emerge into the hypothesised larger-radii, lower-density CSM. If this scenario is correct, our radio observations at 36, 76, and 148 d after explosion should therefore probe ongoing CSM interaction between the fastest-moving ejecta and material lost from the star around 1, 2, and 4 yr before explosion, respectively.

Following Kamble et al. (2014) and Kamble et al. (2016), we adopt the models of Chevalier (1998) to describe the radio flux from SN 2015G at the observed epochs, as-

suming that the radial density profile of the CSM goes as $\rho \propto r^{-2}$ at large radii. We parameterise the energy distribution of the shocked electrons as a power law in the electron Lorentz factor with index p, $n_e(\gamma_e) \propto \gamma_e^{-p}$; we assume that the fractional energy densities in the relativistic electrons and in the magnetic field are equivalent (i.e., the shocked material is in equipartition), $\epsilon_e = \epsilon_B$; and we assume that $\epsilon_e = 0.1$. These models include both the effects of synchrotron self-absorption and free-free absorption from the CSM.

In Figure 10 we plot our 3σ nondetections against modeled radio light curves assuming $v_{\mathrm{wind}} = 1000\,\mathrm{km\,s^{-1}}$ and $v_{\mathrm{shock}} = 10{,}000\,\mathrm{km\,s^{-1}}$. We show models for a range of values for the wind parameter, $10^{0.8} \leq A_* \leq 10^{1.7}$, where

$$A_* \equiv \frac{\dot{M}/10^{-5}\,\mathrm{M_\odot\,yr^{-1}}}{v_{\mathrm{wind}}/10^3\,\mathrm{km\,s^{-1}}}$$

Our first epoch of observations produces the strongest constraint on the wind mass-loss rate from SN 2015G's progenitor: $\dot{M} \lesssim 1 \times 10^{-4}\,M_\odot\,yr^{-1}$. Assuming a slower wind velocity produces a more stringent constraint (we find $\dot{M} \lesssim 10^{-5}\,\mathrm{M_\odot\,yr^{-1}}$ if $v_{\mathrm{wind}} = 100\,\mathrm{km\,s^{-1}}$), while assuming a slower shock velocity relaxes the constraint (we find $\dot{M} \lesssim 10^{-3}\,\mathrm{M_\odot\,yr^{-1}}$ if $v_{\mathrm{shock}} = 5000\,\mathrm{km\,s^{-1}}$).

Radio emission from SNe Ibn is still uncharted territory, and it is difficult to know whether the assumptions (and therefore the models) outlined above are fully appropriate. Similar assumptions have been shown to be reasonable for stripped-envelope SNe with detected radio light curves, but the diversity of radio signatures found for these events is remarkable, especially among the SNe with evidence for unsteady pre-explosion mass loss from their progenitor. See, for example, PTF 11qcj, a radio-bright SN Ic that may have had a SN 2006jc-like outburst from its progenitor ~ 2 yr before core collapse (Corsi et al. 2014), or SN 2014C, a SN Ib that began to interact with an H-rich dense shell a year after explosion and showed extreme variability in its radio light curve (Margutti et al. 2017).

Our radio flux limits and the resultant CSM density limits shown in Figure 10 are surprising, given the strong signatures of a dense CSM at low radii — SNe Ib/c with ra-
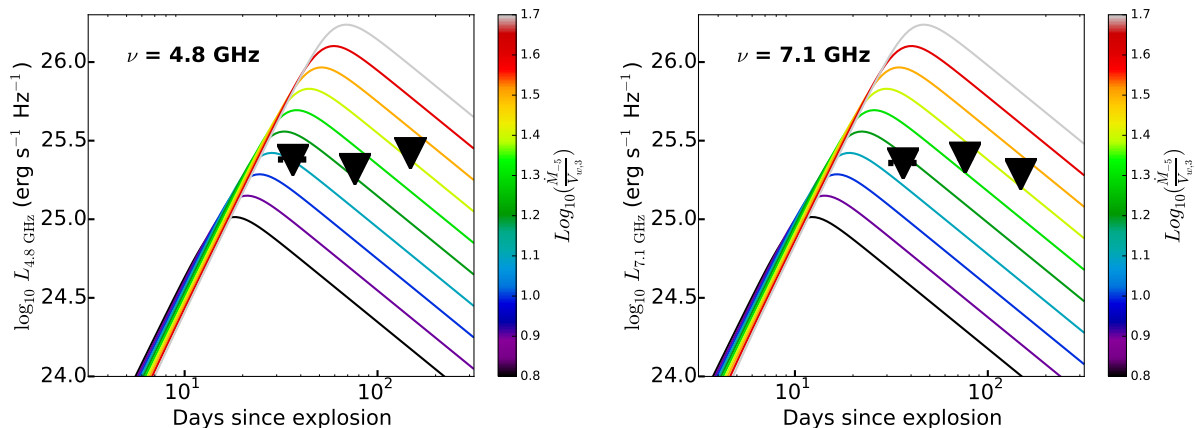
Figure 10. Our 3σ nondetections of SN 2015G at 4.8 and 7.1 GHz, plotted against modeled light curves assuming a range of values for the wind parameter. These models were constructed assuming $v_{\text{shock}} = 10,000\,\text{km s}^{-1}$ and $v_{\text{wind}} = 1000\,\text{km s}^{-1}$. We adopt an explosion date of 57080 MJD, and we show horizontal error bars of $\pm 5\,\text{d}$ to illustrate our uncertainty about the exact date of explosion (the plotted data points are often wider than those error bars).

dio detections generally have peak luminosities in the range 10^{26}–$10^{28}\,\text{erg s}^{-1}\,\text{Hz}^{-1}$ at these frequencies (e.g., Soderberg 2007). If the CSM around SN 2015G had a structured density profile at large radii, perhaps with shells of material created by episodes of eruptive mass loss rather than the steady wind-driven profile we model above, the radio emission powered by ongoing interaction could be entirely obscured via free-free absorption within the CSM exterior to the shock. Type IIn SNe in very dense environments, for example, sometimes exhibit radio light curves with rise times of $\sim 1000\,\text{d}$ because of this effect (e.g., Chandra et al. 2012, 2015). These SNe sustain the optical signatures of ongoing interaction, however, while SN 2015G's narrow spectral features disappear and its interaction-powered optical brightness fades away — differences which argue that the radial profile of the CSM surrounding SN 2015G must be quite dissimilar from the (relatively) smooth density profiles inferred for the SNe IIn above. A further worry is that our models do not account for any CSM clumpiness or global asymmetry, though our optical observations argue that the SN 2015G system is strongly asymmetric. Without clear detections and lacking a true radio light curve, many uncertainties remain.

3.7 Progenitor Constraints

SN 2015G is the nearest known SN Ibn to date, and as such it provides us a unique opportunity to study the progenitor star and local environment for a member of this rare subclass. A preliminary search for the progenitor in the *HST*/WFPC2 images from 2001 was presented by Maoz & Poznanski (2015). They established the SN position in these archival pre-SN data using a ground-based *I*-band image and did not detect a progenitor candidate there. Neglecting any extinction within the host galaxy, they estimate upper limits on the luminosity of a progenitor at $M_I > -6.4$ mag and $M_V > -7.1$ mag.

We initially used our *HST* Target of Opportunity (ToO) WFC3 images from GO-13683 to provide a better position for the SN in the 2001 WFPC2 *F555W* data. However, since the individual frame times for the ToO observations were only 10 s each (for a total of 240 s) and we observed in sub-array mode, there were only 7 stars in common between the two image datasets. Consequently, we could only register the images with a 1σ uncertainty of 0.61 WF pixel (the SN site is on the WF2 chip of the WFPC2 array). We therefore registered the pre-SN images to the much deeper WFC3 full-array data from GO-14149 (total exposure times of 780 s in *F555W*, 710 s in *F814W*). We found 30 star-like objects in common between the images and were able to achieve an astrometric registration that was somewhat better, with a 1σ uncertainty of 0.38 WF pixel. We note that the positions for the SN in the pre-SN data estimated from the two different WFC3 image sets agree to 0.49 pixel. We also do not see a progenitor candidate at this position, nor does DOLPHOT detect any object there. In Figure 11 we present the *HST*/WFC3 image of SN 2015G from November 2015, a close-up view of the SN and its local environment, and a close-up view of the progenitor nondetection from 2001 (all in the *F814W* band).

As Figure 11 shows, SN 2015G exploded far from the bulk of the stellar mass in NGC 6951 and far from the major star-forming regions. As noted by Maoz & Poznanski (2015), however, there is a small but conspicuous clump of bright and blue stars near that location. The centre of this clump is $\sim 2''$ west of SN 2015G, a distance of $\sim 200\,\text{pc}$. Most of the stars in the clump are within $\sim 100\,\text{pc}$ of the centre — if SN 2015G's progenitor formed as a part of this clump, it appears to have traveled an appreciable distance from its birthplace. Alternatively, the progenitor may have formed within a smaller stellar subgroup, possibly at a different time.

Our final spectrum of SN 2015G was observed with this cluster along the slit, and a narrow H I line arising from this small star-forming region was detected. The redshift as measured from this emission line is in good agreement with the published redshift of the host galaxy, with an observed wavelength of $6592.33 \pm 0.06\,\text{Å}$ (as measured via maximum-likelihood MCMC fitting, assuming a Gaussian line profile). This implies a redshift of 0.00450, or a line-of-sight velocity within $100\,\text{km s}^{-1}$ of that of NGC 6951.

We attempted artificial-star tests with DOLPHOT on the
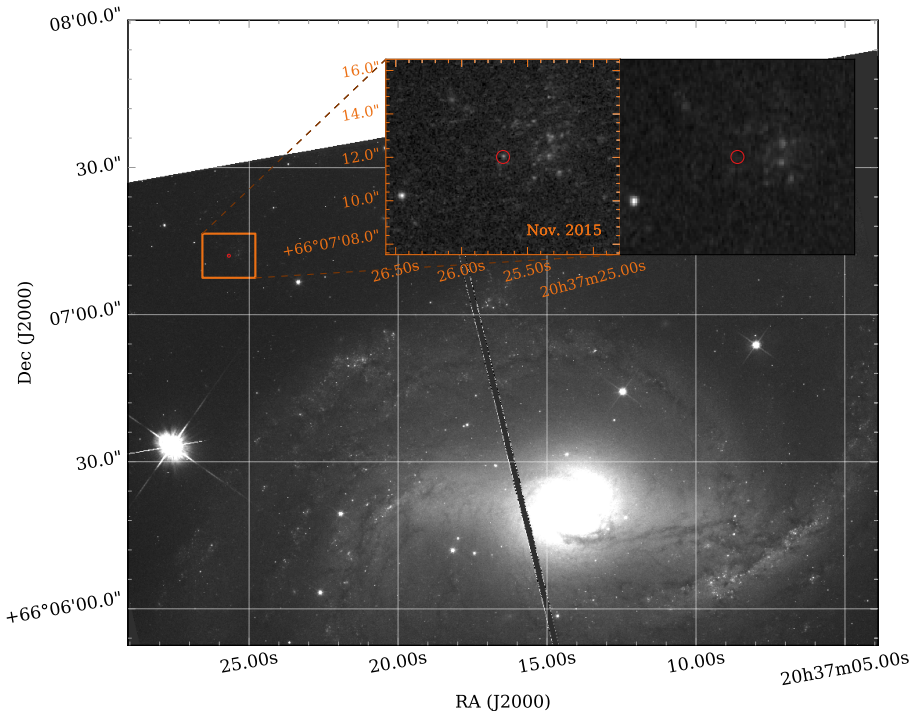
Figure 11. *HST* image of SN 2015G taken ~ 8 months after discovery and a pre-explosion image of the SN site from 2001, both observed through the *F814W* filter. The main frame shows the large offset between SN 2015G and its host, while the two inset frames display close-up views of the fading SN (left) and the pre-explosion progenitor nondetection (right). We indicate the location of the SN using a red circle with a radius of 0.3″ (larger than our 3σ uncertainty in the SN location).

images from 2001, injecting an artificial star at the exact SN position, and found the following nondetection upper limits: $F555W \gtrsim 26.7$ mag and $F814w \gtrsim 25.4$ mag. These are consistent with the formal 3σ source detections by `DOLPHOT` at the SN's location, and they translate into absolute upper limits of $M_{F555W} \gtrsim -6.4$ mag and $M_{F814W} \gtrsim -7.1$ mag. These limits are essentially the same as those found by Maoz & Poznanski (2015), though their assumptions of the distance and reddening to the SN differed from ours.

Assuming the progenitor of SN 2015G was a single supergiant, and that it exploded at the terminus of its evolutionary track as something other than a hydrogen-rich supergiant, we compared our detection upper limits with the MESA Isochrones and Stellar Tracks (MIST; Paxton et al. 2011, 2013, 2015; Choi et al. 2016) at solar and slightly subsolar ([Fe/H] = −0.25) metallicities, adjusted for the distance and reddening to SN 2015G as described above. We find the following limits on the zero-age main sequence mass by comparison with our $F555W$ limit (the more constraining of the two): $M_0 \lesssim 18\,M_\odot$ (solar) and $M_0 \lesssim 20\,M_\odot$ (subsolar). These limits effectively rule out a single massive ($M_0 \gtrsim 30\,M_\odot$) Wolf-Rayet star progenitor (assuming that the luminosity at the time of collapse is similar to the luminosities observed for Wolf-Rayet stars in the MW). Comparisons, instead, with the interacting binary models of Kim et al. (2015) show that some configurations are disallowed by our upper limits but a variety of possible binary models remain viable. Note that *HST* images of the field were obtained in 1994 through the *F218W* and *F547M* filters, but they do not provide deeper constraints.

Maund et al. (2016) have recently reported the likely detection of a binary companion to the progenitor of SN 2006jc in *HST* images obtained 4 yr after the SN explosion. The pre-explosion upper limits we find for the progenitor system of SN 2015G are marginally consistent with a similarly luminous source, depending upon the assumed properties of the extinction along the line of sight within the host galaxy.

We also considered the stellar environment of SN 2015G to constrain the properties of the progenitor. We analyzed objects within a 43-pixel (~ 200 pc) radius of the SN detected by `DOLPHOT` in the WFC3 *F555W* and *F814W* images from GO-14149 that had a `DOLPHOT` object type of "1" (i.e., starlike). The resulting colour-magnitude diagram is shown in Figure 12. We again compared the stellar photometry to the MIST tracks and found that, assuming that the population of stars in this region are coeval and that the SN progenitor itself was not rejuvenated in its evolution as a result of binary interaction, the highest initial mass the progenitor star could have had was ~ 18 $M_\odot$, consistent with the upper limits calculated from our progenitor nondetection.

Comparing our Figure 11 to Figure 1 of Maund et al. (2016), we note the remarkable similarity between SN 2006jc's local environment and that of SN 2015G: both SNe exploded in sparse areas of their hosts near clumps of young, massive stars but offset from them by $\gtrsim 100$ pc. The Type IIn SN 2009ip was also quite isolated (Smith et al. 2016), and Smith & Tombleson (2015) show that luminous blue variables (LBVs) in the MW, often proposed to be Galactic analogues for the progenitors of strongly interacting SNe, are as well. They interpret the isolation of LBVs as evidence that they are mass gainers in binary pairs which get rejuvenated by mass exchange and receive a kick when their (more massive) companion explodes, allowing them to travel far from their birth sites before their own deaths (note that these results are under some debate; e.g., Humphreys et al. 2016).

The presence of a dense CSM surrounding SN 2015G suggests a recent history of extreme mass loss from, and
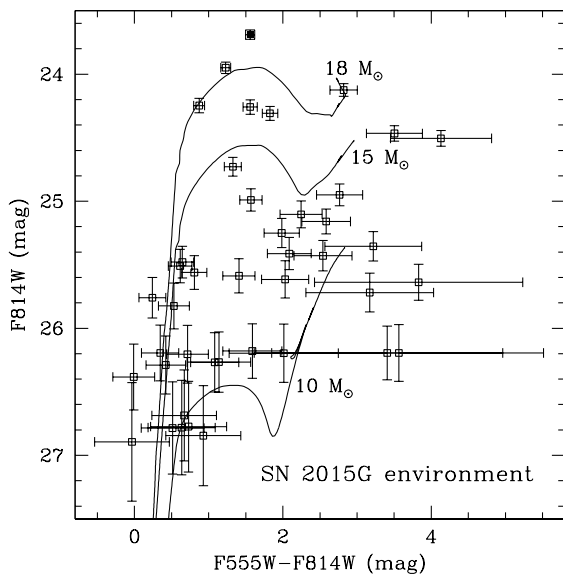
Figure 12. Colour-magnitude diagram of star-like objects (open squares) detected by `DOLPHOT` within a 43-pixel (~ 200 pc) radius of SN 2015G's position in *HST*/WFC3 images obtained in 2015 by program GO-14149. The SN itself is shown as a filled square. For comparison we plot MIST stellar evolutionary tracks at slightly subsolar ([Fe/H] = −0.25) metallicity and initial masses of 10, 15, and 18 $M_\odot$, adjusted to the assumed distance and reddening of SN 2015G.
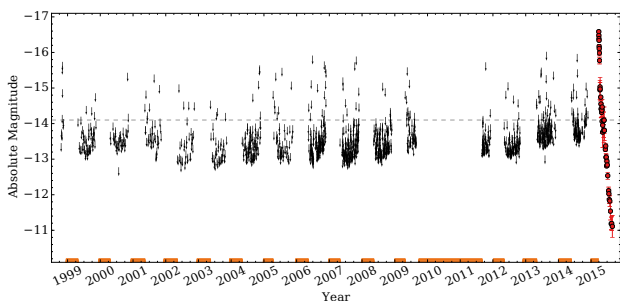
Figure 13. Our 1σ pre-explosion nondetections from KAIT unfiltered images. The *R*-band light curve of SN 2015G is shown at the far right. Timespans for which no upper limit had been obtained for at least 1 month are marked in orange along the bottom, and a dashed line indicates the absolute magnitude of SN 2006jc's pre-explosion outburst (Foley et al. 2007).

therefore variability of, the progenitor star. An LBV-like bright outburst from SN Ibn 2006jc's progenitor was observed some 2 yr before the SN itself ($M_r \approx -14.1$ mag; Nakano et al. 2006; Foley et al. 2007; Pastorello et al. 2007). There have also been a few SN IIn progenitors detected in outburst in the years prior to core collapse (e.g., Mauerhan et al. 2013; Margutti et al. 2014; Smith 2014; Ofek et al. 2014), though similar outbursts have, in other cases, been ruled out (e.g., Bilinski et al. 2015). KAIT has been monitoring NGC 6951 for almost 20 yr and we searched this extensive dataset for evidence of pre-explosion variability.

Examining 1248 unfiltered images taken between 1998 and 2015 with detectability thresholds deeper than 17.0 mag,

we find no detections at the SN location and no evidence for previous outbursts of the progenitor brighter than -13.3 ± 0.5 mag (median and standard deviation of the detection thresholds among all images). Figure 13 plots our 1σ nondetections and the observed light curve of SN 2015G, with the luminosity of SN 2006jc's pre-explosion outburst indicated for comparison. (The *HST* nondetections described above provide additional extremely strong constraints in 2001 May, off the bottom of the scale of Figure 13.) The SN field was inaccessible to our telescopes for several months every year, so there are significant gaps; the orange bars along the bottom of Figure 13 mark every night on which more than 1 month had passed since the previous upper limit. Approximately 45% of the nights between October 1998 and the SN discovery in March 2015 fall into such a gap.

Though these observations rule out any long-lasting luminous outbursts in the last 20 yr, the outburst from SN 2006jc's progenitor was observed to fade rapidly after discovery (~ 0.16 mag d^{-1} over the 9 d it was detected, Pastorello et al. 2007); thus, our nondetections argue neither for nor strongly against a SN 2006jc-like outburst from SN 2015G's progenitor (Nakano et al. 2006; Pastorello et al. 2007).

3.8 A Rough Schematic of the SN 2015G System

Based upon the above observations, we interpret SN 2015G to be a Type Ib SN explosion modified by additional luminosity arising via the collision between explosive ejecta and dense CSM, with the collision between SN ejecta and the CSM converting the kinetic energy of the ejecta into radiative luminosity (e.g., Chugai & Danziger 1994; Chevalier & Fransson 1994; Chevalier & Irwin 2011).

The luminous yet rapidly fading light-curve peak settles into a slower decline rate, while either ongoing (weaker) interaction or a (relatively small amount of) radioactive material powers the luminosity of the late-time light-curve tail. Our spectroscopic monitoring of SN 2015G began after shock breakout and peak luminosity, and the early-time spectra of the event show a cooling blue continuum topped by relatively broad emission lines (arising from the ejecta and perhaps the shocked and accelerated CSM) and narrow P-Cygni lines (arising from the unshocked and extended CSM at larger radii which has been ionized by the shock breakout). The spectral lines at early phases are centred at a velocity of 0 km s^{-1}, and therefore the CSM in which these early lines formed likely exhibited a range of velocity vectors more or less symmetrically distributed around the progenitor.

These narrow P-Cygni features disappeared from our spectra ~ 10 d after the discovery of SN 2015G, or ~ 35 d after our roughly estimated explosion date. Coupled with our radio nondetections (the first of which was observed 36 d post-explosion), this argues that the dense CSM was predominantly located at small radii and was therefore likely lost from the surface of the progenitor in the last year or so before core collapse.

As the light curve settles into its late-time decline rate, the broader features transition from pure emission into a P-Cygni profile, likely arising from some mixture of the swept-up CSM and the ejecta. The light curve then continues to decline steadily as the continuum, and therefore the absorption features, fade away. As the ejecta and ac-

celerated CSM continue to expand and the density drops, forbidden emission lines become prominent. The evolution of all emission lines redward argues that the line flux at late times arises predominantly within receding material, unlike the early emission-line flux.

Whether ongoing weak CSM interaction or a relatively small amount of ^{56}Ni powers the late-time light curves of SNe Ibn is still a difficult question. SN 2015G's late-time decline at redder wavelengths (the *I* and *F814W* passbands) appears to be very similar to that at bluer wavelengths (*V* and *F555W*), arguing that the blue pseudocontinuum and the (mostly red) emission lines are powered by the same process. The blue pseudocontinuum is generally understood to be powered via CSM interaction, and so this argues that the line emission also arises from CSM interaction.

In contrast, the linear decline of the late-time light curve and the homogeneity of light-curve shapes among SNe Ibn argue for the radioactively powered interpretation. If SN Ibn light curves are interaction-powered on the tail, the diversity of late-time light-curve properties should reflect the diversity of CSM configurations around the progenitors; it would be surprising if these CSM configurations (and therefore the progenitor pre-explosion mass-loss histories) were so similar across different SNe (e.g., Pastorello et al. 2008a; Hosseinzadeh et al. 2017). The light curves of SNe IIn (which assuredly are powered largely by interaction) are very heterogeneous, as expected (e.g., Kiewe et al. 2012), though comparisons with hydrogen-rich SNe must be made with caution; the lack of hydrogen in SNe Ibn may force the continuum opacity significantly lower. Note that the late-time luminosities of SNe Ibn are low compared to those of normal SNe Ib/Ic — if they are radioactively powered at late times, it seems they must produce a relatively small amount of ^{56}Ni.

The systemic redshift of the CaII and HeI lines implies a severe (and peculiar) asymmetry of the system, likely due to an asymmetry of the CSM with which SN 2015G's ejecta are interacting at these phases (assuming these lines are interaction-powered). However, we do observe some polarization intrinsic to SN 2015G at early times, and a less-than-spherical explosion itself may also be playing a role. Not only are asymmetric geometries often invoked to understand the observed properties of core-collapse SNe (e.g., Mazzali et al. 2005; Maeda et al. 2008; Modjaz et al. 2008; Taubenberger et al. 2009; Milisavljevic et al. 2010), but both the analysis of some SN remnants and the results of modern 2- and 3-dimensional modeling efforts of the core-collapse mechanism itself argue that asymmetric (sometimes unipolar) explosions are possible and may even be common.

The Puppis A SN remnant (Petre et al. 1996), for example, shows a compact neutron-star remnant with a systemic velocity of some $1000\,\mathrm{km\,s^{-1}}$ along a vector opposite that of the bulk ejecta velocity, arguing that the neutron star received a substantive kick from the core-collapse event and that the ejecta received a similar kick in the opposite direction. Explosion asymmetries of lesser degree have also been observed (e.g., the so-called "Bochum" event of SN 1987A; Phillips & Heathcote 1989). From the modeling side, several teams have shown that low-order spherical harmonics of the exploding core may well manifest themselves in large-scale asymmetries of the explosion (e.g., Suwa et al. 2010; Hanke et al. 2012; Couch & Ott 2014; Couch & O'Connor 2014).

4   CONCLUSION

SN 2015G, which exploded in NGC 6951 at a distance of 23.2 Mpc, is the nearest known SN Ibn to date. Though it was discovered after peak brightness, we have been able to accrue a remarkable dataset on this event, making it one of the best-studied SNe of this rare type and highlighting both strong similarities with and differences from the archetypical SN Ibn 2006jc.

Hosseinzadeh et al. (2017) argue for two spectroscopically defined subclasses of SNe Ibn, but our observations of SN 2015G show that it exhibited properties of both proposed subclasses. Rather than two physically distinct subclasses, perhaps a continuum of CSM properties surrounding the SN produces a continuum of spectroscopic properties; this question should be investigated further as more SNe Ibn are identified and studied.

Archival *HST* images of the resolved SN explosion site argue against a single massive WR-like progenitor for SN 2015G. Given the recent likely detection of a binary companion to SN 2006jc's progenitor, the isolation of SN 2015G's explosion site and the well-determined position of the SN in multiple *HST* images makes SN 2015G an excellent candidate for a similar study in the future.

The data presented here argue that extreme mass loss from the progenitor of SN 2015G occurred soon (~ 1 yr) before core collapse, and that the SN 2015G system was asymmetric. Asymmetries in stripped-envelope SNe are common, but the degree of asymmetry shown by the late-time spectra of SN 2015G has not been observed in a SN Ibn before now. A dedicated effort to obtain more high-resolution spectra and better late-time coverage of SNe Ibn is called for to understand whether severe asymmetry is characteristic of SNe Ibn or a unique trait of the SN 2015G system.

grateful to the staffs of Lick, Keck, and the other observatories where we obtained data for their excellent assistance.

REFERENCES

Arnett W. D., 1971, ApJ, 163, 11

Bilinski C., Smith N., Li W., Williams G. G., Zheng W., Filippenko A. V., 2015, MNRAS, 450, 246

Blondin S., Tonry J. L., 2007, ApJ, 666, 1024

Breeveld A. A., Landsman W., Holland S. T., Roming P., Kuin N. P. M., Page M. J., 2011, in McEnery J. E., Racusin J. L., Gehrels N., eds, American Institute of Physics Conference Series Vol. 1358, American Institute of Physics Conference Series. pp 373–376 (arXiv:1102.4717), doi:10.1063/1.3621807

Brown P. J., Breeveld A. A., Holland S., Kuin P., Pritchard T., 2014, Ap&SS, 354, 89

Byard P. L., O'Brien T. P., 2000, in Iye M., Moorwood A. F., eds, Proc. SPIE Vol. 4008, Optical and IR Telescope Instrumentation and Detectors. pp 934–941, doi:10.1117/12.395415

Chandra P., Chevalier R. A., Chugai N., Fransson C., Irwin C. M., Soderberg A. M., Chakraborti S., Immler S., 2012, ApJ, 755, 110

Chandra P., Chevalier R. A., Chugai N., Fransson C., Soderberg A. M., 2015, ApJ, 810, 32

Chevalier R. A., 1998, ApJ, 499, 810

Chevalier R. A., Fransson C., 1994, ApJ, 420, 268

Chevalier R. A., Irwin C. M., 2011, ApJ, 729, L6

Choi J., Dotter A., Conroy C., Cantiello M., Paxton B., Johnson B. D., 2016, ApJ, 823, 102

Chugai N. N., 2009, MNRAS, 400, 866

Chugai N. N., Danziger I. J., 1994, MNRAS, 268, 173

Colgate S. A., White R. H., 1966, ApJ, 143, 626

Corsi A., et al., 2014, ApJ, 782, 42

Couch S. M., O'Connor E. P., 2014, ApJ, 785, 123

Couch S. M., Ott C. D., 2014, in American Astronomical Society Meeting Abstracts #223. p. 216.05

Dolphin A. E., 2000, PASP, 112, 1383

Drout M. R., et al., 2011, ApJ, 741, 97

Faber S. M., et al., 2003, in Iye M., Moorwood A. F. M., eds, Proc. SPIE Vol. 4841, Instrument Design and Performance for Optical/Infrared Ground-based Telescopes. pp 1657–1669, doi:10.1117/12.460346

Filippenko A. V., 1982, PASP, 94, 715

Filippenko A. V., Li W. D., Treffers R. R., Modjaz M., 2001, in Paczynski B., Chen W.-P., Lemme C., eds, Astronomical Society of the Pacific Conference Series Vol. 246, IAU Colloq. 183: Small Telescope Astronomy on Global Scales. p. 121

Filippenko A. V., Chornock R., Swift B., Modjaz M., Simcoe R., Rauch M., 2003, IAU Circ., 8159

Fisher A. K., 2000, PhD thesis, THE UNIVERSITY OF OKLAHOMA

Foley R. J., 2015, MNRAS, 452, 2463

Foley R. J., Smith N., Ganeshalingam M., Li W., Chornock R., Filippenko A. V., 2007, ApJ, 657, L105

Foley R. J., Zheng W., Filippenko A. V., Dyk S. D. V., 2015, The Astronomer's Telegram, 7298

Ganeshalingam M., et al., 2010, ApJS, 190, 418

Ganeshalingam M., Li W., Filippenko A. V., 2013, MNRAS, 433, 2240

Gehrels N., et al., 2004, ApJ, 611, 1005

Guillochon J., Parrent J., Kelley L. Z., Margutti R., 2016, preprint, (arXiv:1605.01054)

Hanke F., Marek A., Müller B., Janka H.-T., 2012, ApJ, 755, 138

Haynes M. P., van Zee L., Hogg D. E., Roberts M. S., Maddalena R. J., 1998, AJ, 115, 62

Heiles C., 2000, AJ, 119, 923

Hosseinzadeh G., et al., 2017, ApJ, 836, 158

Humphreys R. M., Weis K., Davidson K., Gordon M. S., 2016, ApJ, 825, 64

Kamble A., et al., 2014, ApJ, 797, 2

Kamble A., et al., 2016, ApJ, 818, 111

Kasliwal M. M., et al., 2012, ApJ, 755, 161

Kiewe M., et al., 2012, ApJ, 744, 10

Kim H.-J., Yoon S.-C., Koo B.-C., 2015, ApJ, 809, 131

Krist J. E., Hook R. N., Stoehr F., 2011, in Optical Modeling and Performance Predictions V. p. 81270J, doi:10.1117/12.892762

Leonard D. C., Filippenko A. V., Chornock R., Foley R. J., 2002, PASP, 114, 1333

Li W., Filippenko A. V., Van Dyk S. D., Hu J., Qiu Y., Modjaz M., Leonard D. C., 2002, PASP, 114, 403

Li W., et al., 2011, MNRAS, 412, 1441

Liu Y., Modjaz M., 2014, preprint, (arXiv:1405.1437)

Lucy L. B., 1991, ApJ, 383, 308

Lunnan R., et al., 2017, ApJ, 836, 60

Maeda K., et al., 2008, Science, 319, 1220

Maoz D., Poznanski D., 2015, The Astronomer's Telegram, 7563

Margutti R., et al., 2014, ApJ, 780, 21

Margutti R., et al., 2017, ApJ, 835, 140

Matheson T., Filippenko A. V., Chornock R., Leonard D. C., Li W., 2000, AJ, 119, 2303

Mauerhan J. C., et al., 2013, MNRAS, 430, 1801

Mauerhan J. C., et al., 2015, MNRAS, 453, 4467

Maund J. R., Pastorello A., Mattila S., Itagaki K., Boles T., 2016, ApJ, 833, 128

Mazzali P. A., et al., 2005, Science, 308, 1284

Meixner M., et al., 2008, in Ground-based and Airborne Instrumentation for Astronomy II. p. 70142W, doi:10.1117/12.790224

Milisavljevic D., Fesen R. A., Gerardy C. L., Kirshner R. P., Challis P., 2010, ApJ, 709, 1343

Milisavljevic D., et al., 2015, ApJ, 815, 120

Miller J., Stone R., 1993, Lick Observatory Techical Reports, 66

Modjaz M., Kirshner R. P., Blondin S., Challis P., Matheson T., 2008, ApJ, 687, L9

Nakano S., Itagaki K., Puckett T., Gorelli R., 2006, Central Bureau Electronic Telegrams, 666

Ofek E. O., et al., 2014, ApJ, 789, 104

Oke J. B., et al., 1995, PASP, 107, 375

Pastorello A., et al., 2007, Nature, 447, 829

Pastorello A., et al., 2008a, MNRAS, 389, 113

Pastorello A., et al., 2008b, MNRAS, 389, 131

Pastorello A., et al., 2015a, MNRAS, 449, 1921

Pastorello A., et al., 2015b, MNRAS, 454, 4293

Pastorello A., et al., 2016, MNRAS, 456, 853

Paxton B., Bildsten L., Dotter A., Herwig F., Lesaffre P., Timmes F., 2011, ApJS, 192, 3

Paxton B., et al., 2013, ApJS, 208, 4

Paxton B., et al., 2015, ApJS, 220, 15

Perets H. B., et al., 2010, Nature, 465, 322

Peri C. S., Benaglia P., Isequilla N. L., 2015, A&A, 578, A45

Petre R., Becker C. M., Winkler P. F., 1996, ApJ, 465, L43

Phillips M. M., Heathcote S. R., 1989, PASP, 101, 137

Phillips M. M., et al., 2013, ApJ, 779, 38

Piascik A. S., Steele I. A., Bates S. D., Mottram C. J., Smith R. J., Barnsley R. M., Bolton B., 2014, in Ground-based and Airborne Instrumentation for Astronomy V. p. 91478H, doi:10.1117/12.2055117

Podsiadlowski P., Joss P. C., Hsu J. J. L., 1992, ApJ, 391, 246

Poole T. S., et al., 2008, MNRAS, 383, 627

Poznanski D., Prochaska J. X., Bloom J. S., 2012, MNRAS, 426, 1465

Quataert E., Shiode J., 2012, MNRAS, 423, L92

Rockosi C., et al., 2010, in Ground-based and Airborne Instrumentation for Astronomy III. p. 77350R, doi:10.1117/12.856818

Roming P. W. A., et al., 2005, Space Sci. Rev., 120, 95

Sakon I., et al., 2009, ApJ, 692, 546

Sana H., et al., 2012, Science, 337, 444

Sanders N. E., et al., 2013, ApJ, 769, 39

Schlafly E. F., Finkbeiner D. P., 2011, ApJ, 737, 103

Serkowski K., Mathewson D. S., Ford V. L., 1975, ApJ, 196, 261

Shivvers I., et al., 2016a, preprint, (arXiv:1609.02922)

Shivvers I., et al., 2016b, MNRAS, 461, 3057

Silverman J. M., et al., 2012, MNRAS, 425, 1789

Skrutskie M. F., et al., 2006, AJ, 131, 1163

Smith N., 2010, MNRAS, 402, 145

Smith N., 2014, ARA&A, 52, 487

Smith N., Arnett W. D., 2014, ApJ, 785, 82

Smith N., Tombleson R., 2015, MNRAS, 447, 598

Smith N., Foley R. J., Filippenko A. V., 2008, ApJ, 680, 568

Smith N., Li W., Filippenko A. V., Chornock R., 2011, MNRAS, 412, 1522

Smith N., Mauerhan J. C., Silverman J. M., Ganeshalingam M., Filippenko A. V., Cenko S. B., Clubb K. I., Kandrashoff M. T., 2012, MNRAS, 426, 1905

Smith N., Andrews J. E., Mauerhan J. C., 2016, MNRAS, 463, 2904

Soderberg A. M., 2007, in Immler S., Weiler K., McCray R., eds, American Institute of Physics Conference Series Vol. 937, Supernova 1987A: 20 Years After: Supernovae and Gamma-Ray Bursters. pp 492–499 (arXiv:0706.3047), doi:10.1063/1.3682950

Stetson P. B., 1987, PASP, 99, 191

Suwa Y., Kotake K., Takiwaki T., Whitehouse S. C., Liebendörfer M., Sato K., 2010, PASJ, 62, L49

Taubenberger S., et al., 2009, MNRAS, 397, 677

Thomas R. C., Nugent P. E., Meza J. C., 2011, PASP, 123, 237

Weyant A., Wood-Vasey W. M., Allen L., Garnavich P. M., Jha S. W., Joyce R., Matheson T., 2014, ApJ, 784, 105

Yusa T., et al., 2015, Central Bureau Electronic Telegrams, 4087

This paper has been typeset from a TeX/LaTeX file prepared by the author.